

Mean field study of the topological Haldane-Hubbard model of spin-1/2 fermions

V. S. Arun,¹ R. Sohal,¹ C. Hickey,¹ and A. Paramekanti^{1,2}

¹*Department of Physics, University of Toronto, Toronto, Ontario M5S 1A7, Canada and*

²*Canadian Institute for Advanced Research, Toronto, Ontario M5G 1Z8, Canada*

Motivated by exploring the effect of interactions on Chern insulators, and by recent experiments realizing topological bands for ultracold atoms in synthetic gauge fields, we study the honeycomb lattice Haldane-Hubbard model of spin-1/2 fermions. Using an unrestricted mean field approach, we map out the instability of the topological band insulator towards magnetically ordered insulators which emerge with increasing Hubbard repulsion. In addition to the topological Néel phase, we recover various chiral noncoplanar magnetic orders previously identified within a strong coupling approach. We compute the band structure of these ordered phases, showing that the triple- Q tetrahedral phase harbors topological Chern bands with large Chern numbers.

I. INTRODUCTION

Theory and experiments on spin-orbit coupled crystalline solids have shown that they can display various types of nontrivial bulk topological bands,^{1–9} with unusual chiral surface states. Topologically nontrivial Chern bands have also been realized in recent experiments on cold atoms in two-dimensional (2D) lattices, using fermionic ⁴⁰K atoms in a Floquet realization of the honeycomb lattice Haldane model with zero net flux per unit cell,^{10,11} and bosonic ⁸⁷Rb atoms in a Hofstadter model with a net flux of $\pi/2$ per unit cell realized using Raman-assisted tunneling.¹² These developments have led to rejuvenated interest in understanding interaction effects in such topological bands.

Early work on the time-reversal symmetry broken Hofstadter model in an optical lattice showed that interacting bosons could realize lattice analogues of various fractional quantum Hall (FQH) states, e.g., the $\nu = 1/2$ Laughlin liquid, as well as FQH states which have no continuum analogues.^{13–19} More recently, attention has focussed on interaction effects in Chern insulators. These break time-reversal symmetry and support bands with nonzero Chern numbers, but possess full lattice translation symmetry due to *zero* net magnetic flux per elementary lattice unit cell (modulo an integer number of flux quanta per plaquette which can be gauged away). In the regime of nearly flat Chern bands, where such bands mimic continuum Landau levels, interactions have been shown to drive various types of FQH liquids for both spinless bosons and spinless fermions;^{20–25} for recent reviews, see Refs. 26 and 27. Similar issues have been previously studied also for interacting time-reversal invariant topological insulators, such as the Kane-Mele-Hubbard model,^{28–33} as well as more realistic models appropriate to spin-orbit coupled oxides.^{34,35} In these cases it has been found that correlation effects lead to various easy-plane magnetic orders or Z_2 quantum spin liquids.

Here, we study the topological honeycomb lattice Haldane model³⁶ of a quantum anomalous Hall insulator (QAH). Previous work on spinless bosons in this model at fractional filling found evidence for a fractional quantum Hall liquid.²⁵ At integer filling, it was found that weak interactions induce unusual superfluid phases, while strong interactions lead to plaquette Mott insulators with loop currents.³⁷ On the other hand, spinless fermions with nearest neighbor repulsion lead

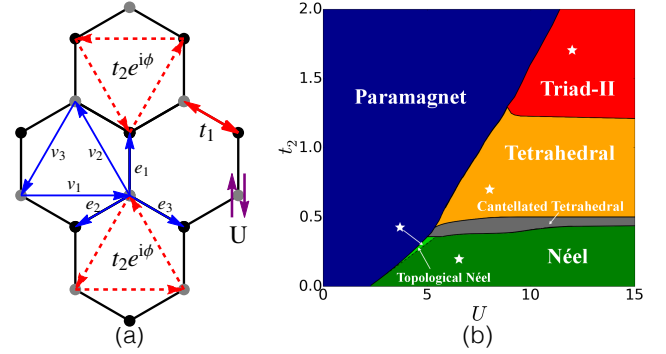


FIG. 1. (Color online) (a) Honeycomb lattice showing the two sublattices, the nearest and next-nearest neighbor lattice vectors $\{e_i\}$ and $\{v_i\}$, the hopping amplitudes t_1, t_2 , phase ϕ and the Hubbard repulsion U of the Haldane-Hubbard model. (b) Mean field phase diagram at $\phi = \pi/2$ showing the various magnetic phases that emerge at finite U . Stars (\star) mark the points at which the mean field band structure is plotted in Figs. 4, 5 and 6.

to a topologically trivial charge-density wave crystal.^{38,39} In recent work, it has been shown that the physics of two-component fermions (i.e., spin-1/2 fermions) in the Haldane-Hubbard model could be far richer.^{40–46} Without interactions, this model has a total Chern number $C = 2$ at a filling of one fermion per site. Within a strong coupling approach, the effective spin model of the Haldane-Mott insulator at this filling hosts chiral three-spin interactions. At the classical level, this model supports nontrivial chiral magnetic orders, including a triple- Q tetrahedral phase; these orders were shown to persist even for spin $S = 1/2$ via an exact diagonalization (ED) study.⁴⁶ Furthermore, ED and density matrix renormalization group (DMRG) computations found that frustration-induced melting of the tetrahedral spin crystal resulted in a chiral spin liquid,^{44,46} the $\nu = 1/2$ bosonic Laughlin liquid with topological degeneracy and gapped semion excitations,^{47–49} This provides an example of a topological Mott insulator^{50–53} in a realistic Hamiltonian.

In this paper, we revisit the Haldane-Hubbard model away from its strong-coupling limit, and obtain the following key results. (i) Using an unrestricted real-space mean field theory of the Hubbard interaction, we examine all possible magnetic instabilities of the paramagnetic QAH in an unbiased manner. Over a small window of parameters, we find the previ-

ously reported topological Néel ordered phase,⁴⁵ which gives way to a topologically trivial Néel phase at larger interaction. More interestingly, and reassuringly, various chiral noncoplanar magnetic orders, such as the triple- Q tetrahedral phase, previously discovered within a strong coupling approach as arising from chiral three-spin interactions in the Mott insulating phase, also appear in this mean field theory. Our study provides estimates for the interaction strength at which the QAH becomes unstable to various broken symmetry insulating phases. While the emergence of noncoplanar chiral magnetic order at moderate coupling agrees with a previous mean-field study of the Haldane-Hubbard model,⁴⁵ the ordering patterns we find in our work are considerably different from Ref. 45 since they focused on a specific ansatz, whereas we do not make any *a priori* assumptions about the unit cell. (ii) Using the converged mean field solution, we compute the band structure and Berry curvature of the various magnetically ordered insulating phases. In the tetrahedral phase, we find that a naïve application of a commonly employed projection approach, which assumes that the itinerant fermions in the ordered phase move adiabatically with spins projected along the local Zeeman field axes,^{54,55} while it is generally a useful approach, is *inadequate* in this case to understand the band dispersion since it produces spurious band touchings due to an artificial restoration of time-reversal symmetry. Our numerical mean field calculations in the tetrahedral phase show that these band touchings in fact get gapped out, and a Berry curvature computation yields robust topological bands with high Chern numbers.

Our work thus sheds light on the interaction-driven instabilities of quantum Hall band insulators towards Mott insulators with exotic magnetic orders, which may ultimately be driven into chiral spin liquids by frustration effects. In some ways, our study is a parallel of previous work on the Kane-Mele-Hubbard model²⁸ where weak and strong coupling approaches were applied to understand the impact of interactions on a 2D time-reversal invariant topological insulator.

How relevant are these results to the ultracold atom experiments which realize the Haldane model as an effective description of a Floquet problem associated with a driven optical lattice? Recent work on interaction effects in driven Hamiltonians have suggested that the Haldane-Hubbard model and its strong coupling limit may be a reasonable description of the physics in the regime where the drive frequency exceeds the Hubbard model parameters, $\Omega \gg U, t$, and further that the heating rate is exponentially small in this regime.⁵⁶⁻⁵⁸ Indeed, the experimentally measured heating rate for interacting two-component fermions appears not to be too large.¹¹ In this case, equilibration in the effective equilibrium description of the interacting Floquet problem could potentially occur (i.e., prethermalization) before the onset of significant heating.⁵⁶⁻⁵⁸ Thus, we expect at least short-range spin correlations of these magnetically ordered states to be visible using techniques such as Bragg scattering^{59,60} and noise measurements.⁶¹

II. MODEL AND MEAN FIELD THEORY

The Haldane-Hubbard model for spin-1/2 fermions shown in Fig. 1(a) is defined by the Hamiltonian

$$H_{\text{HH}} = -t_1 \sum_{\langle ij \rangle \sigma} (c_{i\sigma}^\dagger c_{j\sigma} + h.c.) - t_2 \sum_{\langle\langle ij \rangle\rangle \sigma} (e^{i\nu_{ij}\phi} c_{i\sigma}^\dagger c_{j\sigma} + h.c.) + U \sum_i n_{i\uparrow} n_{i\downarrow}, \quad (1)$$

where $\langle \cdot \rangle$ and $\langle\langle \cdot \rangle\rangle$ denote, respectively, first and second nearest neighbors, $\nu_{ij} = \pm 1$ produces a flux pattern with a net zero flux per unit cell, and U is the Hubbard repulsion.

Without interactions, $U = 0$, this model supports Chern bands for $t_2, \phi \neq 0$. At half-filling, this leads to a QAH with $\sigma_{xy} = \pm e^2/h$ per spin for small $|t_2|$. At large $|t_2|$ and $\phi \neq \pi/2$, the Chern bands strongly disperse, leading to a metal with $\sigma_{xy} \neq 0$ but non-quantized.⁴⁴ In this paper, we will focus attention on the case $\phi = \pi/2$, for which the half-filled state is a QAH for arbitrarily large t_2 . What we would like to explore is the fate of this topological band insulator as we crank up interactions.

For strong interactions, $U \gg t_1, t_2$, and a half-filled lattice with one fermion per site, it is obvious that the ground state is a charge-localized Mott insulator. The effective model describing the residual spin degrees of freedom in the Mott insulator features antiferromagnetic Heisenberg interactions at $\mathcal{O}(t^2/U)$, and nonvanishing chiral three-spin interactions at $\mathcal{O}(t^3/U^2)$, of the type $\mathbf{S}_1 \cdot \mathbf{S}_2 \times \mathbf{S}_3$ on triangular plaquettes. The chiral terms originate from broken time-reversal symmetry. The competition between these two types of interactions in the Mott phase has been shown to lead to a variety of chiral magnetic orders within a classical spin approximation, as well as from ED studies on 32-site clusters.⁴⁶ However, this previous work does not shed light on the interaction strength at which these magnetic orders emerge, or whether truncating the large- U expansion at $\mathcal{O}(t^3/U^2)$ is justified.

Here we therefore explore an alternative route to treating the Hubbard repulsion, using a traditional mean-field decoupling of the local four-fermion interaction into all possible channels, leading to an effective quadratic Hamiltonian. Previous studies along these lines have focussed on only certain types of magnetic orders; here, we carry out a completely unbiased self-consistent study by using a site-dependent mean-field theory on $L \times L$ lattices (with $2L^2$ sites due to having two sites per unit cell) with system sizes upto $L = 12$, backed up by momentum space computations on large lattices. This allows us to recover certain previously identified phases such as a topological Néel phase. In addition, we find large regions of the phase diagram which support various chiral magnetic orders which coincide with those deduced from the strong coupling approach in the Mott insulating phase.

To decompose the Hubbard interaction via a site-dependent Hartree factorization, we define the mean fields $\rho_i = \langle n_i \rangle$ and $\mathbf{m}_i = \frac{1}{2} \langle c_{i\alpha}^\dagger \boldsymbol{\sigma}_{\alpha\beta} c_{i\beta} \rangle$ at each site i , corresponding, respectively, to the local charge density and magnetization. Using these, the

mean field Hamiltonian is

$$H_{\text{MF}} = -t_1 \sum_{\langle ij \rangle \sigma} (c_{i\sigma}^\dagger c_{j\sigma} + h.c.) - t_2 \sum_{\langle\langle ij \rangle\rangle \sigma} (e^{i\nu_{ij}\phi} c_{i\sigma}^\dagger c_{j\sigma} + h.c.) + \frac{U}{2} \sum_i \rho_i \sum_\sigma c_{i\sigma}^\dagger c_{i\sigma} - 2U \sum_i \mathbf{m}_i \cdot \mathbf{S}_i, \quad (2)$$

where we have dropped constant terms. To solve the mean-field theory, we have to demand self-consistency of these mean field parameters $\{\rho_i, \mathbf{m}_i\}$. Denoting the eigenfunctions of H_{MF} as $\Psi_n(i, \sigma)$, this condition reduces to

$$\rho_i = \sum_n \sum_\alpha \Psi_n^*(i, \alpha) \Psi_n(i, \alpha) f(\epsilon_n), \quad (3)$$

$$\mathbf{m}_i = \frac{1}{2} \sum_n \sum_{\alpha\beta} \Psi_n^*(i, \alpha) \sigma_{\alpha\beta} \Psi_n(i, \beta) f(\epsilon_n), \quad (4)$$

where ϵ_n is the energy of the n^{th} eigenstate, and $f(\epsilon_n)$ is the Fermi-Dirac function. Here, we restrict ourselves to zero temperature. We consider a lattice with N honeycomb lattice unit cells, which leads to $2N$ lattice sites and a total of $4N$ single particle states including spin. Thus, at zero temperature, the effect of the Fermi-Dirac function at half-filling amounts to summing n over $2N$ lowest energy states. Furthermore we set $t_1 = 1$ for the remainder of the paper.

We have solved these mean field equations using an iterative self-consistent approach. Starting with an initial random guess for the local mean field parameters $\{\rho_i, \mathbf{m}_i\}$, we diagonalize H_{MF} in real space to find the eigenvalues and eigenvectors. We then use these eigenvectors and energies to compute ρ_i, \mathbf{m}_i via Eqns. 3,4, iterating this process until convergence is reached. In our calculations we considered $L \times L$ lattices (with $2L^2$ sites) with system sizes up to $L = 12$ with periodic boundary conditions. Since the local density rapidly converges to a uniform value of one fermion per site in all cases, we found it suffices to impose the convergence condition on the magnetization $\sum_{i=1}^N |\Delta \mathbf{m}_i| < 10^{-6}$ where $\Delta \mathbf{m}_i$ is the change in \mathbf{m}_i between subsequent iterations. As further checks on the phase diagram, we have used many different random initial conditions to start the self-consistency loop. Furthermore, while H_{MF} in Eq. 2 omitted constant terms which are unimportant for self-consistency, we have reinstated this term to compute the total mean field energy as

$$\langle H \rangle = \sum_{n=1}^{2N} \epsilon_n + U \sum_{i=1}^{2N} (\mathbf{m}_i^2 - \rho_i^2/4). \quad (5)$$

We have explicitly checked that we are selecting ground states with the lowest energy $\langle H \rangle$.

III. MAGNETISM AND BAND TOPOLOGIES

Using the method described in the previous section, we were able to determine the phase diagram shown in Fig. 1(b). In addition to the paramagnetic QAH, it features various magnetic phases which we have labelled as topological Néel,

Néel, tetrahedral, triad-II, and cantellated tetrahedral. Fig. 2 shows the magnetic configuration for the Néel, tetrahedral and triad-II phases. All of the phases were found to have a site-independent density $\rho_i = 1$, so we focus here purely on their magnetic structure.

Once we know the real space magnetic structure we can use the corresponding magnetic unit cell, see Fig. 2, to rewrite the Hamiltonian in momentum space. An example of this approach is given below for the case of Néel order. This approach also dramatically reduces the number of variational degrees of freedom, down to just one parameter in the case of the Néel and tetrahedral, and two parameters in the case of the triad-II. We use the same form of iterative self-consistent approach to determine the parameters as outlined in the previous section. This leads to excellent agreement between the real space and momentum space calculations. Computing the energy of each order directly in momentum space on large lattices allows us to confirm the location of the various phase boundaries in Fig. 1(b). Furthermore, we use this to carry out Berry curvature and Chern number computations of the bands in the various phases, following the numerical procedure outlined by Fukui, Hatsugai and Suzuki.⁶²

A. Paramagnet

The paramagnet corresponds to $\mathbf{m}_i = 0$ and $\rho_i = 1$. In mean field theory, this simply leads back to the non-interacting Haldane model. The inclusion of spin results in four bands, a set of two lower degenerate bands with a combined Chern number $C = -2$ and two upper degenerate bands with $C = 2$. For $t_2 = 0$ the upper and lower bands touch at Dirac points located at $\pm K$. A nonzero t_2 gaps out these band touchings, with the location of the minimum band gap shifting from the $\pm K$ points to the M points for $t_2 > 1/3\sqrt{3}$, as indicated by the dashed white line in Fig. 3.

B. Néel and Topological Néel

The magnetic order in the Néel and Topological Néel states corresponds to collinear spins, aligned antiparallel on the two sublattices of the honeycomb lattice. In this state, $\langle \hat{\chi}_\Delta \rangle = 0$ on all triangular plaquettes, where $\hat{\chi}_\Delta \equiv \mathbf{m}_i \cdot \mathbf{m}_j \times \mathbf{m}_k$ is the scalar spin chirality operator, with the sites $\{ijk\}$ being labeled going anticlockwise around the triangles. Its magnetic structure factor $\mathcal{M}(\mathbf{q}) = \frac{1}{N} \sum_{i,j} \langle \mathbf{m}_i \cdot \mathbf{m}_j \rangle e^{i\mathbf{q} \cdot (\mathbf{r}_i - \mathbf{r}_j)}$ exhibits a Bragg peak at $\mathbf{q} = 0$.

To study the magnetic order in the Néel states in momentum space, we use the unit cell in Fig. 2(a) and orient the spins in the \hat{z} direction. The Fourier transformed Néel Hamiltonian has the form

$$H_{\text{Néel}} = \sum_{\mathbf{k}} \mathbf{c}_{\mathbf{k}}^\dagger \mathcal{M}_{\text{Néel}}(\mathbf{k}) \mathbf{c}_{\mathbf{k}}, \quad (6)$$

where $\mathbf{c}_{\mathbf{k}} = (c_{A,\uparrow}, c_{B,\uparrow}, c_{A,\downarrow}, c_{B,\downarrow})^T$ with A, B representing

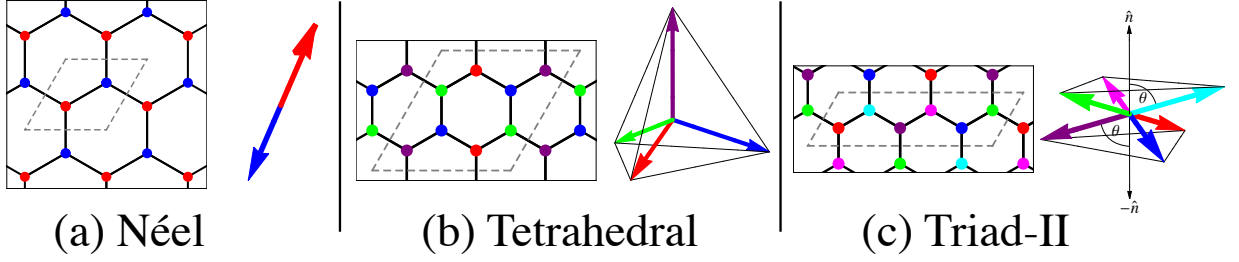


FIG. 2. (Color online) Real space spin structure of the (a) Néel, (b) tetrahedral and (c) triad-II phases. The sites are labelled by colors on the left side of each subfigure with the corresponding spin vector shown on the right side. The dashed lines mark out the magnetic unit cell.

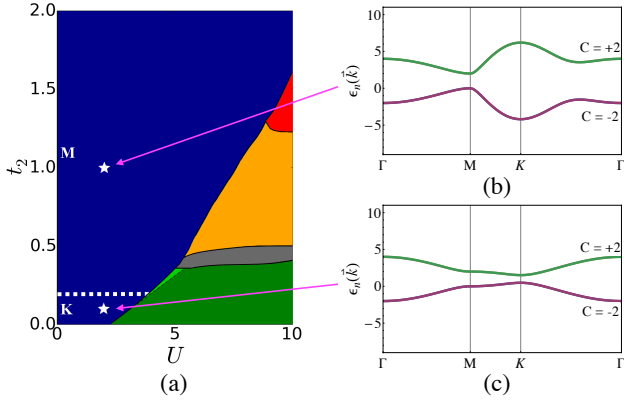


FIG. 3. (Color online) (a) Paramagnetic region of the phase diagram with the smallest band gap lying at the M points above the dashed white line and at $\pm K$ below it. Examples of the band structure are shown at (b) $t_2 = 1.0$ and (c) $t_2 = 0.1$.

the two sublattices. In this basis, \mathcal{M} is block diagonal,

$$\mathcal{M}_{\text{Néel}}(\mathbf{k}) = \begin{pmatrix} \mathbf{h}(\mathbf{k}) \cdot \boldsymbol{\tau} - Um\tau_z & 0 \\ 0 & \mathbf{h}(\mathbf{k}) \cdot \boldsymbol{\tau} + Um\tau_z \end{pmatrix}. \quad (7)$$

Here, we have defined

$$h_x(\mathbf{k}) = -[\cos(\mathbf{k} \cdot \mathbf{e}_1) + \cos(\mathbf{k} \cdot \mathbf{e}_2) + \cos(\mathbf{k} \cdot \mathbf{e}_3)], \quad (8)$$

$$h_y(\mathbf{k}) = -[\sin(\mathbf{k} \cdot \mathbf{e}_1) + \sin(\mathbf{k} \cdot \mathbf{e}_2) + \sin(\mathbf{k} \cdot \mathbf{e}_3)], \quad (9)$$

$$h_z(\mathbf{k}) = -2t_2 [\sin(\mathbf{k} \cdot \mathbf{v}_1) + \sin(\mathbf{k} \cdot \mathbf{v}_2) + \sin(\mathbf{k} \cdot \mathbf{v}_3)], \quad (10)$$

with $\pm m\hat{z}$ being the magnetization on the A, B sublattices, while the lattice unit vectors are given by

$$\mathbf{e}_1 = (0, a); \mathbf{e}_2 = \left(-\frac{\sqrt{3}a}{2}, -\frac{a}{2}\right); \mathbf{e}_3 = \left(\frac{\sqrt{3}a}{2}, -\frac{a}{2}\right), \quad (11)$$

$$\mathbf{v}_1 = (\sqrt{3}a, 0); \mathbf{v}_2 = \left(-\frac{\sqrt{3}a}{2}, \frac{3a}{2}\right); \mathbf{v}_3 = \left(-\frac{\sqrt{3}a}{2}, -\frac{3a}{2}\right). \quad (12)$$

Solving the resulting self-consistent equation for m , we find that the onset of Néel order appears via a continuous transition from the paramagnet, with no closing of a single-particle gap. This transition may be viewed as a condensate of direct excitons formed from particles and holes at the K point (or $-K$ point). Close to the transition, on the ordered side, the

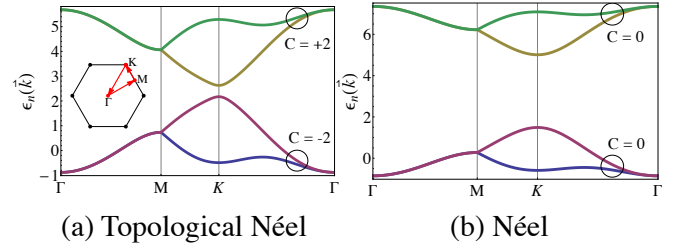


FIG. 4. (Color online) Band structure of the (a) topological Néel phase for $t_2 = 0.3$, $U = 4.8$ and (b) Néel phase for $t_2 = 0.2$, $U = 6.5$ along the high symmetry lines of the honeycomb lattice BZ (shown in the inset). The bands carry a total Chern number $C = \pm 2$ in the topological Néel phase, while $C = 0$ in the Néel phase.

sublattice magnetization \mathbf{m} is small, increasing continuously in magnitude away from the critical point. We can find this critical repulsion for the onset of Néel order by expanding the self-consistent equation to linear order in m , which yields

$$\frac{1}{U_c} = \frac{1}{2L} \sum_{\mathbf{k} \in \text{BZ}} \frac{(h_x^2 + h_y^2)}{|\mathbf{h}|^3} \quad (13)$$

where L^2 is the number of unit cells. When m is small, as we can see from $\mathcal{M}_{\text{Néel}}(\mathbf{k})$ in Eq. 7, it leads to a small sublattice imbalance potential for each spin;⁴⁵ this breaks the spin degeneracy present in the paramagnetic band structure. However, there exists a small window of U over which the topological properties of the paramagnetic bands survive, namely a combined $C = -2$ for the two lower bands and $C = +2$ for the two upper bands. Increasing U drives a gap closing at the $\pm K$ points which makes the combined Chern numbers of both sets of bands trivial. Thus, as noted in Ref. 45, the band structure of the Néel allows us to divide it into topologically trivial and non-trivial phases, with examples for each phase given in Fig. 4. The topological Néel to ordinary Néel transition is a topological transition with a change of band topology but no change in the sublattice magnetisation. However, as pointed out in Ref. 45, fluctuations beyond mean-field theory due to the coexistence of gapless fermions and gapless Néel spin wave modes may render the transition first-order.

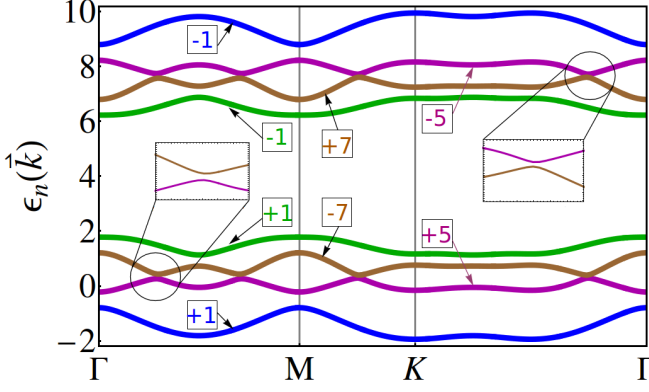


FIG. 5. (Color online) Band structure of the tetrahedral phase for $t_2 = 0.7$, $U = 8$ along the high symmetry lines of the original honeycomb lattice BZ (shown in the inset of Fig. 4(a)). Each band is doubly degenerate and there are no band touchings; since the gaps at a number of points are difficult to resolve by eye, we have magnified a couple of examples. Each set of degenerate bands is labelled by their total Chern number.

C. Tetrahedral

The tetrahedral has spins pointing from the origin towards the four corners of a tetrahedron, and are tiled on the lattice as shown in Fig. 2(b). This non-coplanar state has a uniform chirality $\langle \hat{\chi}_\Delta \rangle$ on each small- Δ formed by two nearest neighbor and one next-nearest neighbor link. The tetrahedral state is a triple- Q state, with the structure factor $\mathcal{M}(\mathbf{q})$ exhibiting Bragg peaks at the M points in the Brillouin zone (BZ). The transition into the tetrahedral state is first order, which we attribute to symmetry-allowed third order chiral terms in a Landau theory formulation; we also confirm this with a direct numerical evaluation of the energy as a function of the magnetization.

The 8-site magnetic unit cell of the tetrahedral results in a total of 16 bands; these form 8 degenerate pairs as seen from Fig. 5 where we have plotted them in the original large BZ of the honeycomb lattice. The pairs of degenerate bands do not intersect each other. This allows us to assign each pair a total Chern number as indicated in Fig. 5, computed using the method outlined in Ref. 62. With increasing U , we find that the gaps between these bands appears to close at a number of points in the BZ. However, the gaps always remain nonzero but are difficult to resolve by eye, as we illustrate in the insets. The existence of these ‘almost band touching’ points can be understood if we appeal to a ‘projection’ approach^{54,55} which assumes that the bands in the magnetically ordered state can be constructed by studying fermions moving adiabatically in the background of the tetrahedral order, while having their spins perfectly polarized along the local Zeeman field axes.

In the projection approach, we ignore the explicit underlying tetrahedral order, instead assuming its effects are encoded in the emergent Berry phase factors^{54,55} for fermions as they traverse closed loops on the honeycomb lattice. Fermions hopping in a closed three-site loop will pick up a Berry phase

of $\pm\pi/2$ corresponding to half the solid angle subtended by any three of the four spins of the tetrahedron. Combined with the Haldane flux $\phi = \pi/2$ this produces an effective flux of $\pm\pi$ through each small triangle as well as a total flux of $\pm\pi$ through each hexagon. This modified flux pattern means that the projected system has an artificial time-reversal symmetry, that is not strictly present in the original Hamiltonian. Thus, the projection approximation cannot lead to isolated gapped bands with nonzero Chern numbers. There are only two other possibilities. (i) It could be that the band structure in this approximation has isolated bands with $C = 0$. However, since this adiabatic approximation is expected to be good at large U , this is at odds with our mean field result. (ii) The bands in this approximation cannot be isolated and lead to band touchings. Indeed, we find that the presence of this artificial symmetry results in spurious symmetry-protected band touching points which coincide with the weakly gapped points in the full calculation shown in Fig. 5. At any finite U , the ‘perfectly polarized’ approximation is inadequate due to small but nonzero mixing with the higher energy states, and this small deviation leads to tiny band gaps which we observe in the full mean field calculation in the mean field tetrahedral phase; a computation of the Berry curvature⁶² in this mean field solution yields the observed Chern bands. This illustrates that the projection approach, while it is widely employed and useful for understanding gapped bands and their topological properties, should be used with care when it results in band touchings.

The tetrahedral state also features bands with high Chern numbers, namely $C = \pm 5$ and $C = \mp 7$. This is mainly due to a concentration of Berry curvature at six points in the BZ along the Γ - K high symmetry line. We associate these large Berry curvature regions with band touchings in the projection approach. Focusing on the middle two pairs of bands in the lower set each point contributes a Berry flux of $\pm 2\pi$, due to the twofold degeneracy, giving a total contribution of $C = \pm 6$ to the total Chern number. For the lower pair this, added to a Berry flux contribution of -2π from the Γ point, results in $C = 5$ while for the upper pair, added to a contribution of $+2\pi$ from Γ and a total of -4π from $\pm K$, results in $C = -7$.

D. Triad-II

The triad-II can be thought of as a cone, or umbrella, state on each triangular A , B sublattice with the common axis of each cone, $\pm\hat{n}$ in Fig. 2(c), aligned anti-parallel and spins making an angle θ with $\pm\hat{n}$ (whereas the case in which the common axes align parallel is referred to as triad-I). It has a net anti-ferromagnetic moment and a structure factor $\mathcal{M}(\mathbf{q})$ exhibiting Bragg peaks at Γ and $\pm K$. Each cone can in general be rotated by an angle φ about $\pm\hat{n}$ with respect to the other. The ground state energy has a weak sinusoidal dependence on φ with minima at $\varphi = (2n+1)\pi/3$, and which goes to zero with increasing U . This differs from the results of the recent classical analysis of the strong-coupling spin model in which the energy of the triad-II is independent of φ .

Fixing $\varphi = \pi/3$ in the momentum space calculations leaves two independent variational parameters, the magnetization per

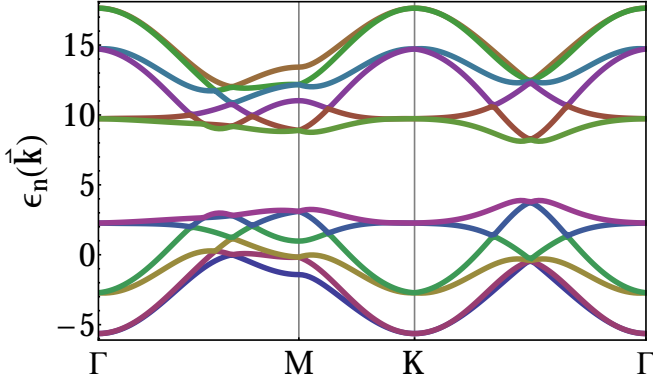


FIG. 6. (Color online) Band structure of the triad-II phase for $t_2 = 1.7$, $U = 12$ along the high symmetry lines of the original honeycomb lattice BZ (shown in the inset of Fig. 4(a)). None of the bands in the lower or upper set are separated in energy and thus it is not meaningful to label the bands with Chern numbers. The total Chern number of the lower (upper) six bands is zero.

site m and the opening angle of the cones, θ . For fixed t_2 the opening angle is an increasing function of U , approaching the limiting value of $\pi/2$ in which the spins on each triangular sublattice form an incommensurate coplanar spiral state. At fixed U the variation of θ with t_2 is relatively negligible for the range of t_2 studied here. We note that, on large system sizes, the triad-II state is expected to be unstable to very weak incommensurate spiralling.⁴⁴

The transition from the paramagnet into the triad-II state is first order, which we again attribute to third order chiral terms in a Landau theory formulation. We have again confirmed with a direct numerical evaluation of the energy.

The 6-site magnetic unit cell of the triad-II results in a total of 12 bands, as shown in Fig. 6 in the original large BZ of the honeycomb lattice. There are no bands separated in energy in the upper/lower set so it is not possible to assign Chern numbers to any one band. The total Chern number of the lower six bands (or upper six bands) is zero.

E. Cantellated Tetrahedral

The Cantellated Tetrahedral (CT) state descends from a parent tetrahedral state. In the parent tetrahedral configuration, the spins marked with a given color in Fig. 2 form a honeycomb lattice, with a larger unit cell. We can deform these ferromagnetically aligned spins by dividing the larger honeycomb lattice into two sublattices, and then allowing for a $\sqrt{3} \times \sqrt{3}$ canting on each sublattice; this splits each vertex of the tetrahedron into six vertices (forming a small hexagon) leading to the CT state with a 24-site unit cell; see Fig. 7.

The CT state exists over a narrow window between the Néel and Tetrahedral states, indicated by the gray region of Fig. 1. The real space self-consistent calculations did not converge to the required accuracy at all the points in the region marked as Cantellated Tetrahedral. However on repeating the calculations using this phase as the initial condition, the algorithm

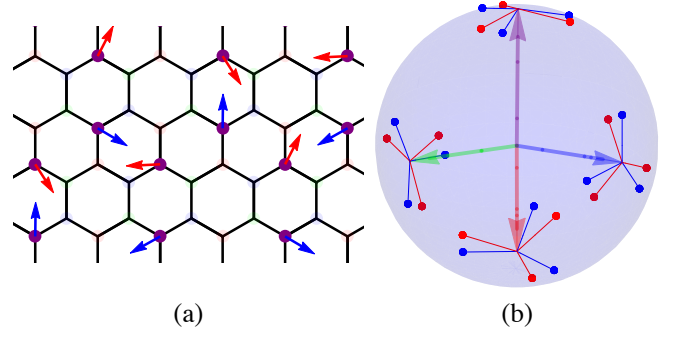


FIG. 7. (Color online) In the tetrahedral state, the spins pointing towards the four vertices of the tetrahedron each reside on their own honeycomb lattice in real space, in (a) the purple dots highlight the sites corresponding to one of the vertices. In the cantellated tetrahedral each tetrahedral vertex splits into six points, with the spins residing on one (e.g. purple) sublattice developing nonzero transverse (tangential) components, shown by the red/blue arrows in (a). These transverse components form 120 degree ordered states on the two triangular sublattices of the purple honeycomb lattice. In (b) the points correspond to the vertices of the cantellated tetrahedral order, with the blue/red color distinguishing the two sublattices of the honeycomb lattice and the arrows indicating parent tetrahedral vertices.

converged at many more points within the gray region to the CT phase. Even at points within the gray region where the solution did not converge to the desired accuracy, the resulting magnetic configuration closely resembled that of the CT phase even though it was not precisely the same, and the energies of these states were lower than that of the other phases. We thus tentatively associate the CT phase with the entire gray region. Due to uncertainties associated with this state, the small window over which it might appear, and the much larger size of its unit cell, we have not further explored its bands and their topological character.

IV. COMPARISON WITH PREVIOUS WORK

We have explored the possible density and magnetic instabilities of the half-filled Haldane-Hubbard model. Using large, unbiased site-dependent mean field theory calculations in real space lattices, we have uncovered a variety of magnetic orders, Néel, cantellated tetrahedral, tetrahedral and triad-II. The non-coplanar orders found in our study differ from 45, since that work only explored a limited ansatz, whereas we do not make any such assumptions. Our ordered phases are in good agreement with those found in recent classical and ED studies of the effective spin model that emerges from a strong coupling approach.^{44,46} (although the cantellated tetrahedral could not be identified in the ED study due to the size of the finite clusters used). As U increases even further, the chiral terms that appear in the spin model at $\mathcal{O}(t^3/U^2)$ become much weaker, and the effective spin model tends towards the J_1 - J_2 model on the honeycomb lattice. Classically this model has Néel and coplanar spiral ground states which again match

with our mean-field results on the Hubbard model at much larger values of U .

Although the mean-field approach captures the magnetic orders seen in the strong coupling limit it cannot be relied upon to completely capture the physics near the Mott transition into magnetically ordered insulating states. Spin and charge fluctuations beyond mean field theory may modify the nature of these transitions, as pointed out in Ref. 45 for the case of the topological Néel to Néel transition - this transition is continuous in our mean field calculations but is predicted to be driven first-order by fluctuation effects. The transitions from the paramagnetic QAHI into the tetrahedral and triad states are found to be first-order in our calculations, driven by cubic chiral terms; this result is unlikely to be qualitatively affected by the inclusion of beyond-mean-field fluctuations.

V. SUMMARY

In summary, we have explored the unconventional magnetic structures found in the Haldane-Hubbard model, and explored

the band structure of the resulting phases. This allows us to identify when the paramagnetic quantum Hall insulator becomes unstable to magnetically ordered insulators, to uncover the topologically non-trivial region of the Néel phase as well as the high Chern numbers of the tetrahedral phase, and to make connections with previous studies of this model in the strong coupling limit.

Note Added: After submission of this work for publication, some recent works have appeared Refs. 63–65 which study the Haldane-Hubbard model using different approximations such as dynamical mean field theory and the variational cluster approximation. In particular, Ref. 65 studies the effect of sub-lattice potential imbalance which we have not considered in our work, and finds the emergence of an interaction-induced $C = 1$ Chern insulator.

Acknowledgements. We thank L. Cincio, R. Desbuquois, G. Jotzu, and Z. Papic for useful discussions. We acknowledge support from NSERC of Canada.

-
- ¹ M. Z. Hasan and C. L. Kane, *Rev. Mod. Phys.* **82**, 3045 (2010).
 - ² X.-L. Qi and S.-C. Zhang, *Rev. Mod. Phys.* **83**, 1057 (2011).
 - ³ M. König, S. Wiedmann, C. Brune, A. Roth, H. Buhmann, L. W. Molenkamp, X.-L. Qi, and S.-C. Zhang, *Science* **318**, 766 (2007).
 - ⁴ D. Hsieh, D. Qian, L. Wray, Y. Xia, Y. S. Hor, R. J. Cava, and M. Z. Hasan, *Nature* **452**, 970 (2008).
 - ⁵ L. X. Yang, Z. K. Liu, Y. Sun, H. Peng, H. F. Yang, T. Zhang, B. Zhou, Y. Zhang, Y. F. Guo, M. Rahn, D. Prabhakaran, Z. Hussain, S. K. Mo, C. Felser, B. Yan, and Y. L. Chen, *Nat Phys* **11**, 728 (2015).
 - ⁶ B. Q. Lv, N. Xu, H. M. Weng, J. Z. Ma, P. Richard, X. C. Huang, L. X. Zhao, G. F. Chen, C. E. Matt, F. Bisti, V. N. Strocov, J. Mesot, Z. Fang, X. Dai, T. Qian, M. Shi, and H. Ding, *Nat Phys* **11**, 724 (2015).
 - ⁷ S.-Y. Xu, N. Alidoust, I. Belopolski, Z. Yuan, G. Bian, T.-R. Chang, H. Zheng, V. N. Strocov, D. S. Sanchez, G. Chang, C. Zhang, D. Mou, Y. Wu, L. Huang, C.-C. Lee, S.-M. Huang, B. Wang, A. Bansil, H.-T. Jeng, T. Neupert, A. Kaminski, H. Lin, S. Jia, and M. Zahid Hasan, *Nat Phys* **11**, 748 (2015).
 - ⁸ C.-Z. Chang, W. Zhao, D. Y. Kim, H. Zhang, B. A. Assaf, D. Heiman, S.-C. Zhang, C. Liu, M. H. W. Chan, and J. S. Moodera, *Nat Mater* **14**, 473 (2015).
 - ⁹ A. J. Bestwick, E. J. Fox, X. Kou, L. Pan, K. L. Wang, and D. Goldhaber-Gordon, *Phys. Rev. Lett.* **114**, 187201 (2015).
 - ¹⁰ W. Zheng and H. Zhai, *Phys. Rev. A* **89**, 061603 (2014).
 - ¹¹ G. Jotzu, M. Messer, R. Desbuquois, M. Lebrat, T. Uehlinger, D. Greif, and T. Esslinger, *Nature* **515**, 237 (2014).
 - ¹² M. Aidelsburger, M. Lohse, C. Schweizer, M. Atala, J. T. Barreiro, S. Nascimbene, N. R. Cooper, I. Bloch, and N. Goldman, *Nat Phys* **11**, 162 (2015).
 - ¹³ E. J. Mueller, *Phys. Rev. A* **70**, 041603 (2004).
 - ¹⁴ A. S. Sørensen, E. Demler, and M. D. Lukin, *Phys. Rev. Lett.* **94**, 086803 (2005).
 - ¹⁵ R. N. Palmer and D. Jaksch, *Phys. Rev. Lett.* **96**, 180407 (2006).
 - ¹⁶ M. Hafezi, A. S. Sørensen, E. Demler, and M. D. Lukin, *Phys. Rev. A* **76**, 023613 (2007).
 - ¹⁷ R. N. Palmer, A. Klein, and D. Jaksch, *Phys. Rev. A* **78**, 013609 (2008).
 - ¹⁸ G. Möller and N. R. Cooper, *Phys. Rev. Lett.* **103**, 105303 (2009).
 - ¹⁹ R. O. Umucalılar and E. J. Mueller, *Phys. Rev. A* **81**, 053628 (2010).
 - ²⁰ D. N. Sheng, Z.-C. Gu, K. Sun, and L. Sheng, *Nat Commun* **2**, 389 (2011).
 - ²¹ N. Regnault and B. A. Bernevig, *Phys. Rev. X* **1**, 021014 (2011).
 - ²² E. Tang, J.-W. Mei, and X.-G. Wen, *Phys. Rev. Lett.* **106**, 236802 (2011).
 - ²³ K. Sun, Z. Gu, H. Katsura, and S. Das Sarma, *Phys. Rev. Lett.* **106**, 236803 (2011).
 - ²⁴ T. Neupert, L. Santos, C. Chamon, and C. Mudry, *Phys. Rev. Lett.* **106**, 236804 (2011).
 - ²⁵ Y.-F. Wang, Z.-C. Gu, C.-D. Gong, and D. N. Sheng, *Phys. Rev. Lett.* **107**, 146803 (2011).
 - ²⁶ S. A. Parameswaran, R. Roy, and S. L. Sondhi, *Comptes Rendus Physique* **14**, 816 (2013).
 - ²⁷ E. J. Bergholtz and Z. Liu, *International Journal of Modern Physics B* **27**, 1330017 (2013).
 - ²⁸ S. Rachel and K. Le Hur, *Phys. Rev. B* **82**, 075106 (2010).
 - ²⁹ D. Zheng, G.-M. Zhang, and C. Wu, *Phys. Rev. B* **84**, 205121 (2011).
 - ³⁰ M. Hohenadler, T. C. Lang, and F. F. Assaad, *Phys. Rev. Lett.* **106**, 100403 (2011).
 - ³¹ C. Griset and C. Xu, *Phys. Rev. B* **85**, 045123 (2012).
 - ³² H.-H. Hung, L. Wang, Z.-C. Gu, and G. A. Fiete, *Phys. Rev. B* **87**, 121113 (2013).
 - ³³ M. Hohenadler, Z. Y. Meng, T. C. Lang, S. Wessel, A. Muramatsu, and F. F. Assaad, *Phys. Rev. B* **85**, 115132 (2012).
 - ³⁴ A. Rüegg and G. A. Fiete, *Phys. Rev. Lett.* **108**, 046401 (2012).
 - ³⁵ T. Liu, B. Douçot, and K. Le Hur, *Phys. Rev. B* **88**, 245119 (2013).
 - ³⁶ F. D. M. Haldane, *Phys. Rev. Lett.* **61**, 2015 (1988).
 - ³⁷ I. Vasić, A. Petrescu, K. Le Hur, and W. Hofstetter, *Phys. Rev. B* **91**, 094502 (2015).

- ³⁸ C. N. Varney, K. Sun, M. Rigol, and V. Galitski, *Phys. Rev. B* **82**, 115125 (2010).
- ³⁹ C. N. Varney, K. Sun, M. Rigol, and V. Galitski, *Phys. Rev. B* **84**, 241105 (2011).
- ⁴⁰ J. He, S.-P. Kou, Y. Liang, and S. Feng, *Phys. Rev. B* **83**, 205116 (2011).
- ⁴¹ J. He, Y.-H. Zong, S.-P. Kou, Y. Liang, and S. Feng, *Phys. Rev. B* **84**, 035127 (2011).
- ⁴² J. Maciejko and A. Rüegg, *Phys. Rev. B* **88**, 241101 (2013).
- ⁴³ D. Prychynenko and S. D. Huber, ArXiv e-prints (2014), [arXiv:1410.2001](#).
- ⁴⁴ C. Hickey, P. Rath, and A. Paramekanti, *Phys. Rev. B* **91**, 134414 (2015).
- ⁴⁵ W. Zheng, H. Shen, Z. Wang, and H. Zhai, *Phys. Rev. B* **91**, 161107 (2015).
- ⁴⁶ C. Hickey, L. Cincio, Z. Papić, and A. Paramekanti, ArXiv e-prints (2015), [arXiv:1509.08461](#).
- ⁴⁷ P. W. Anderson, *Mater. Res. Bull.* **8**, 153 (1973).
- ⁴⁸ V. Kalmeyer and R. B. Laughlin, *Phys. Rev. Lett.* **59**, 2095 (1987).
- ⁴⁹ X. G. Wen, *International Journal of Modern Physics B* **04**, 239 (1990).
- ⁵⁰ D. Pesin and L. Balents, *Nat Phys* **6**, 376 (2010).
- ⁵¹ S. Bhattacharjee, Y. B. Kim, S.-S. Lee, and D.-H. Lee, *Phys. Rev. B* **85**, 224428 (2012).
- ⁵² M. Kargarian, A. Langari, and G. A. Fiete, *Phys. Rev. B* **86**, 205124 (2012).
- ⁵³ J. Maciejko, V. Chua, and G. A. Fiete, *Phys. Rev. Lett.* **112**, 016404 (2014).
- ⁵⁴ J. Ye, Y. B. Kim, A. J. Millis, B. I. Shraiman, P. Majumdar, and Z. Tešanović, *Phys. Rev. Lett.* **83**, 3737 (1999).
- ⁵⁵ T. M. McCormick and N. Trivedi, *Phys. Rev. A* **91**, 063609 (2015).
- ⁵⁶ D. Abanin, W. De Roeck, F. Huveneers, and W. W. Ho, ArXiv e-prints (2015), [arXiv:1509.05386](#).
- ⁵⁷ M. Bukov, M. Kolodrubetz, and A. Polkovnikov, ArXiv e-prints (2015), [arXiv:1510.02744](#).
- ⁵⁸ D. A. Abanin, W. De Roeck, and W. W. Ho, ArXiv e-prints (2015), [arXiv:1510.03405](#).
- ⁵⁹ T. A. Corcovilos, S. K. Baur, J. M. Hitchcock, E. J. Mueller, and R. G. Hulet, *Phys. Rev. A* **81**, 013415 (2010).
- ⁶⁰ R. A. Hart, P. M. Duarte, T.-L. Yang, X. Liu, T. Paiva, E. Khatami, R. T. Scalettar, N. Trivedi, D. A. Huse, and R. G. Hulet, *Nature* **519**, 211 (2015).
- ⁶¹ E. Altman, E. Demler, and M. D. Lukin, *Phys. Rev. A* **70**, 013603 (2004).
- ⁶² T. Fukui, Y. Hatsugai, and H. Suzuki, *Journal of the Physical Society of Japan* **74**, 1674 (2005).
- ⁶³ J. Wu, J. P. Latyr Faye, D. Sénéchal, and J. Maciejko, ArXiv e-prints (2015), [arXiv:1512.04498](#).
- ⁶⁴ Z.-L. Gu, K. Li, and J.-X. Li, ArXiv e-prints (2015), [arXiv:1512.05118](#).
- ⁶⁵ T. I. Vanhala, T. Siro, L. Liang, M. Troyer, A. Harju, and P. Törmä, ArXiv e-prints (2015), [arXiv:1512.08804](#).